Nanoclusters

Yuanyuan Li,[a] John J. Rehr,[b] Ralph G. Nuzzo[c] and Anatoly I. Frenkel[a,d]*

[a]Department of Materials Science and Chemical Engineering, Stony Brook University, Stony Brook, NY 11794, USA, [b]Department of Physics, University of Washington, Seattle, WA 98195, USA, [c]Department of Chemistry, University of Illinois, Urbana, IL 61801, USA, and [d]Division of Chemistry, Brookhaven National Laboratory, Upton, NY 11973, USA. *Correspondence e-mail: anatoly.frenkel@stonybrook.edu

Metal clusters comprise an important class of functional nanomaterials due to their tuneable size, structure, shape and support, which are key factors that affect their physicochemical properties and functions. In cluster research, the main objectives are the design of new materials with the desired properties and the development of new methods for characterizing these materials. In this chapter, methods of extended X-ray absorption fine-structure (EXAFS) analysis developed in the last two decades for the structural characterization of monometallic and bimetallic nanoclusters are reviewed.

1. Introduction

Clusters with sizes ranging from subnanometre to 10 nm in diameter have attracted broad interest due to their non-bulk-like properties. For example, the continuous band structure of metals breaks up into discrete electronic states when the particle size approaches the Fermi wavelength of an electron (Johnston, 2002). For small clusters, multiple absorption peaks are assigned to single-electron intraband resonances, and due to this some clusters exhibit strong fluorescence emission upon UV photoexcitation, which makes them good candidates for biolabels and light-emitting sources (Lin *et al.*, 2009). These properties of small clusters cannot be simply described by scaling laws, and more complicated size-dependent relationships should be considered. Other important physical parameters that do not have analogues in bulk crystalline counterparts are geometry, electronic/atomic structure, shape and composition, all of which have a significant influence on cluster properties.

Additionally, the properties of clusters can be affected by their surroundings, such as ligands, organic solvents, supports and gases, and this environment is often sensitive to, and thus can change as a result of, the operating conditions. Such a sensitivity to the surroundings provides opportunities for producing materials with novel properties (Gates, 1995) and, simultaneously, provides challenges for both experimental and theoretical methods in linking the properties of clusters to their size, shape, structure and composition. For example, electron-microscopy (EM) methods are commonly utilized to image clusters, but their resolving power greatly diminishes when time-resolved measurements (Zheng *et al.*, 2009) or/and realistic catalytic environments (Hansen *et al.*, 2002) are required. These requirements pose the same challenges to X-ray photoelectron spectroscopy (XPS), although the availability of high-flux X-rays based on synchrotron radiation and recent advances in instrumentation have enabled XPS measurements at ambient pressure (Tao *et al.*, 2008) and at the liquid–solid interface (Brown *et al.*, 2013).
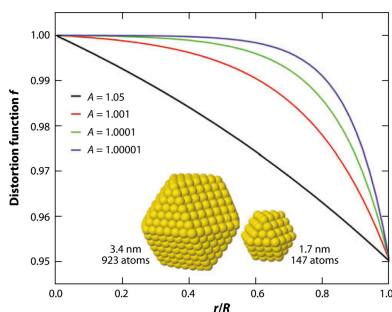
Table 1
Total number of A–A bonds (N_{AA}), total number of A atoms (N_A) and average coordination number (n_1) for several cluster geometries expressed as a function of cluster order L.

The expressions for the cuboctahedron, icosahedron, body-centred cube and simple cube refer to Montejano-Carrizales *et al.* (1997). The expressions for the hemispherical cuboctahedron were generated by Li *et al.* (2015).

Cluster geometry	N_{AA}	N_A	n_1
Cuboctahedron	$4L(5L^2+3L+1)$	$10\dfrac{L^3}{3}+5L^2+11\dfrac{L}{3}+1$	$\dfrac{24L(5L^2+3L+1)}{10L^3+15L^2+11L+3}$
Icosahedron	$20L^3+15L^2+7L$	$10\dfrac{L^3}{3}+5L^2+11\dfrac{L}{3}+1$	$\dfrac{6L(20L^2+15L+7)}{10L^3+15L^2+11L+3}$
Body-centred cube	$8L^3$	$(2L+1)(L^2+L+1)$	$\dfrac{16L^3}{(2L+1)(L^2+L+1)}$
Simple cube	$6L(2L+1)^2$	$(2L+1)^3$	$\dfrac{12L^3}{2L+1}$
Hemispherical cuboctahedron	$10L^3+\dfrac{21}{2}L^2+7\dfrac{L}{2}$	$5\dfrac{L^3}{3}+4L^2+10\dfrac{L}{3}+1$	$\dfrac{3(20L^3+21L^2+7L)}{5L^3+12L^2+10L+3}$
Truncated octahedron	$4L^3+18L^2+26L-12$	$2\dfrac{L^3}{3}+4L^2+25\dfrac{L}{3}$	$\dfrac{12(2L^3+9L^2+13L-6)}{2L^3+12L^2+25L}$

Other techniques such as X-ray diffraction and small-angle X-ray scattering can also provide information about particle size, but those methods work best for particles with sizes larger than several nanometres. X-ray absorption spectroscopy (XAS) can easily adapt to *in situ*/*operando* modes (Frenkel *et al.*, 2014). Compared with EM-based techniques, which probe a few hundreds to thousands of particles, XAS provides excellent statistical information owing to the large fluxes (10^{10}–10^{13} photons per second interrogating the sample) available at today's synchrotrons. XAS detects local structure, which makes it ideal for the investigation of small (less than 2–5 nm in dimeter) clusters where large disorder is expected.

In the rest of this chapter, we will review XAS methods (owing to space limitation, we focus on the extended X-ray absorption fine structure only) developed in recent decades for characterizing the structure of monometallic and bimetallic clusters.

2. Application of EXAFS to monometallic clusters

Fourier-transformed (FT) EXAFS spectra exhibit one or more peaks corresponding to the contributions of different photoelectron paths that connect the absorbing atom and its neighbouring atoms. In the most commonly used form of EXAFS analysis, these paths are characterized by three structure-related parameters that are unique for each path and can be quantified by fitting the theoretical EXAFS spectrum to experimental data. They are the coordination number (CN), the bond distance (R) and the mean-squared bond-length disorder, also known as the EXAFS Debye–Waller factor (σ^2). Among these the CN is a key parameter that is used for the determination of the size and shape of well defined clusters. It is defined as

$$n_i = \frac{2N_{AA(i)}}{N_A}. \qquad (1)$$

Here, N_A is the total number of A-type atoms in the cluster, $N_{AA(i)}$ is the total number of A–A nearest-neighbour pairs within the same coordination shell and n_i is the coordination number of the ith shell at radius R_i around the absorbing atom in a monometallic cluster.

For small monometallic clusters, EXAFS spectra usually show one prominent peak in *r*-space located between 2 and 3 Å. This peak, which depending on the type of absorbing atom can be split into two or more peaks owing to Ramsauer–Townsend resonance (McKale *et al.*, 1988; Rehr *et al.*, 1994), corresponds to the first nearest-neighbour (1NN) metal–metal bond. Basing on the CN of this bond, several methods are available for size determination. One such method was proposed by Montejano-Carrizales *et al.* (1997), who found that N_{AA}, the total number of atoms N_A and the coordination number n_1 of regular polyhedra can be analytically expressed as a function of cluster order (L), which is defined as the number of spacings between adjacent atoms along the edge of the cluster. By comparing n_1 obtained from EXAFS analysis against model structures with known geometrical characteristics (Table 1 and Fig. 1), the size/geometry of the clusters under investigation can be estimated.

Calvin and coworkers developed another useful method to approximate the size of spherical clusters (Calvin *et al.*, 2003). In this method, the average CN of the ith shell (n_i) for the cluster can be written as

$$n_i(\text{nano}) = \left[1 - \frac{3}{4}\left(\frac{r_i}{R}\right) + \frac{1}{16}\left(\frac{r_i}{R}\right)^3\right]N_i(\text{bulk}). \qquad (2)$$

In equation (2), N_i is the ith-shell CN of the bulk structure, r_i is the scattering path length for the ith shell and R is the radius of the cluster. The advantages of this approach are (i) the cluster radius can be directly extracted from the fit and (ii) it also takes into account single scattering paths at higher distances. Indeed, no matter how narrow the cluster size distribution is, the size/geometry of the clusters cannot be obtained only with knowledge of the first nearest CN because of the correlation between the cluster size and shape in terms of their effects on the 1NN coordination numbers. To address this issue, Frenkel and coworkers proposed the utilization of the different

functional behaviours of the 1NN, 2NN, 3NN, 4NN and 5NN coordination numbers as a function of cluster size for studying ideal polyhedral clusters (Frenkel, 1999; Frenkel *et al.*, 2001; Nashner *et al.*, 1997). For instance, knowledge of the 1NN CN is not sufficient to distinguish between a 55-atom icosahedron and a 79-atom truncated octahedron. The degeneracy of the 1NN CNs will be lifted when comparing n_2 or even n_3 owing to their uniqueness for each of these two geometries, as shown in Fig. 1(*b*).

For irregular geometries of relaxed clusters, analytical calculations cannot be performed. Frenkel and coworkers proposed the use of a histogram-based method in which a radial distribution function (RDF) of nearest-neighbouring shells is calculated for any given set of atomic coordinates and the CNs are then obtained by integrating the RDF within the shells of interest (Frenkel *et al.*, 2005; Glasner & Frenkel, 2007). This method is not limited by the shapes and symmetries of a very small number of regular polyhedral clusters, making it a very robust strategy for size/geometry determination.

When the analysis of EXAFS data extends beyond the 1NN contribution, multiple-scattering (as demonstrated in Fig. 2) effects should be included in the model. Using multiple-scattering analysis, Frenkel and coworkers were able to identify the icosahedral geometry of a monolayer-protected Au_{13} cluster (Frenkel *et al.*, 2007; Menard *et al.*, 2006) and determine the shapes of well defined supported nanoclusters (Frenkel, 1999; Frenkel *et al.*, 2001; Roldan Cuenya *et al.*, 2010).

Jentys also proposed the estimation of the mean size and shape of clusters by comparing a set of CNs obtained by EXAFS analysis with those of models with different geometries (Jentys, 1999). This method uses a hyperbolic function to correlate the relationship between the average CN of the *i*th $(1 \leq i \leq 5)$ shell and the total atom number in an f.c.c. cluster,

$$n_i = \frac{aN_A}{b + N_A} + \frac{cN_A}{d + N_A}. \tag{3}$$

Using the known information on 13-atom to 7500-atom clusters, *a*, *b*, *c* and *d* were quantified by applying a nonlinear
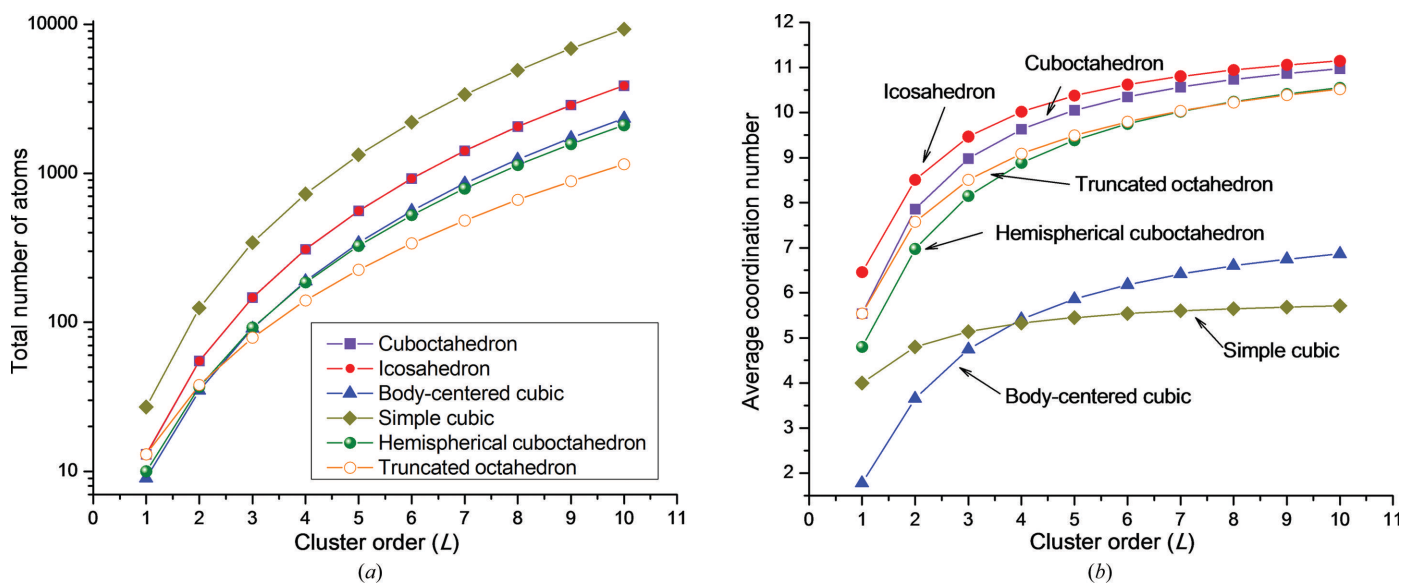

Figure 1
Cluster order L ($0 \leq L \leq 10$) dependent changes of the total number of atoms and average coordination number for a cuboctahedron, icosahedron, body-centred cube, simple cube, hemispherical cuboctahedron and truncated octahedron.
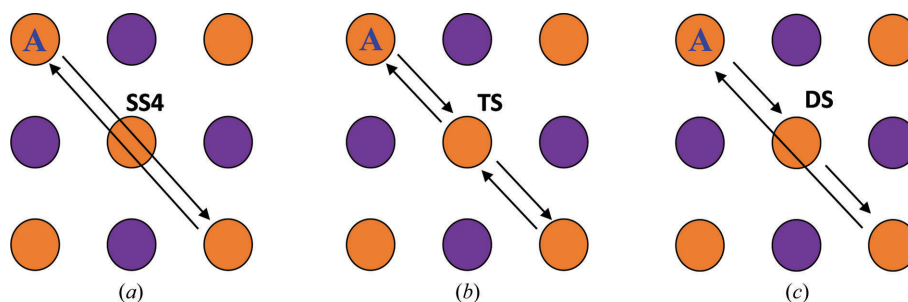

Figure 2
Demonstration of (*a*) fourth-nearest single-scattering (SS4), (*b*) collinear focusing triple-scattering (TS) and (*c*) collinear focusing double-scattering (DS) paths in a face-centred cubic lattice. In each figure, the absorbing atom is labelled 'A', orange atoms are in plane and purple atoms are located above the plane.

least-squares fitting. The particle shape was found to have a minor influence on the CNs of the first and second nearest shells but a significant influence on those of the higher shells. Therefore, one can first estimate the cluster size by using n_1 and further determine the cluster shape by comparing the ratio of n_3 to n_1. A similar idea has been extended by Beale and Weckhuysen to a larger number of atom packings and shapes with the use of the Hill function (Beale & Weckhuysen, 2010).

3. Application of XAFS to bimetallic clusters

3.1. Determination of the composition patterns of bimetallic clusters

Heterometallic clusters composed of two or more metals are of great interest in a broad range of fields (Ganguly *et al.*, 2013; Sasaki *et al.*, 2011; Sun *et al.*, 2000; Tao *et al.*, 2008). The most important factors affecting their properties are the size, morphology and mixing patterns of the different elements in the cluster. Several analytical methods developed based on EXAFS data for characterizing heterometallic nanoclusters will be described here.

In nanoclusters, just as in bulk alloys, one should discriminate between homogeneity and randomness. Both characteristics can be carefully characterized by EXAFS (Frenkel, 2012; Frenkel *et al.*, 2013). Different types of bimetallic configurations are demonstrated in Fig. 3. Compared with the cluster in Fig. 3(*a*), which has perfect short-range (and long-range) order, the atomic distribution is random for the cluster in Fig. 3(*b*). For such random alloys (in which A and B are mixed statistically), n_{AA} and n_{AB} have the same ratio as the bulk concentrations of A and B atoms in the cluster,

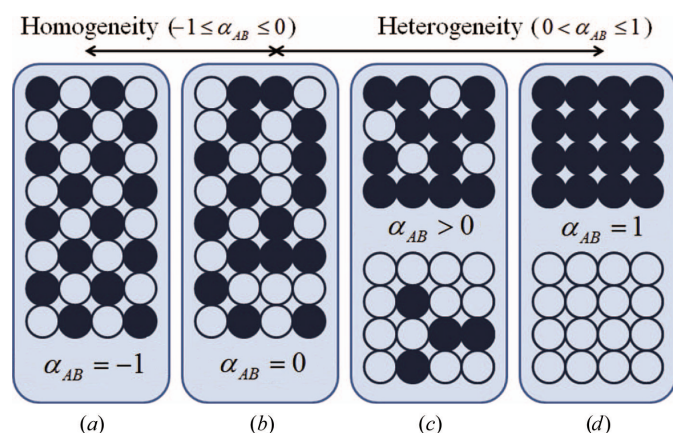$$\frac{n_{AA}}{n_{AB}} = \frac{x_A}{x_B}. \tag{4}$$

Figure 3
(*a*) and (*b*) show homogeneous configurations for the same 50:50 composition characterized by unique, nonpositive values of the short-range order parameter α. Different heterogeneous configurations, characterized by positive values of α, are shown in (*c*) and (*d*). Reprinted from Frenkel *et al.* (2013), with the permission of AIP Publishing.

In equation (4), analogously to the definition of the coordination number for a homometallic pair, the coordination number for heterometallic bonds is defined as

$$n_{AB} = \frac{N_{AB}}{N_A}. \tag{5}$$

In addition, it is also important to compare the average CN of the A–metal (AM) pairs n_{AM} with that of the B–metal (B) pairs n_{BM}. These indices are defined as $n_{AM} = n_{AA} + n_{AB}$, $n_{BM} = n_{BA} + n_{BB}$.

By analysing EXAFS data, the CNs of AM and BM pairs can be obtained, and information about the patterns of mixing or segregation of alloying elements can be analysed by modelling. If $n_{AM} < n_{BM}$, and if the cluster size and composition distribution is narrow, then this inequality points to the preferential location of A atoms near the surface, with smaller numbers of nearest neighbours, while B atoms are preferentially located in the cluster core, where the CN of the nearest neighbours is larger.

For a more formal characterization of segregation or mixing tendencies, including characterization of the randomness of well mixed alloys, we introduce a short-range order parameter α (Frenkel, 2012; Frenkel *et al.*, 2013), similar to its definition by Cowley for bulk alloys (Cowley, 1950),

$$\alpha = 1 - \frac{n_{AB}/n_{AM}}{x_B}. \tag{6}$$

As shown in Fig. 3, α ($-1 \leq \alpha \leq 1$) can be applied to clusters with different degrees of homogeneity and randomness. For alloys that favour or disfavour clustering of like atoms, α will be positive or negative, respectively. In two dimensions, it is -1 for systems with perfect order, zero for random alloys and 1 for systems without the formation of a heterometallic bond. This parameter is therefore essential for the characterization of nanoalloys, such as core-shell, random or cluster-on-cluster types.

In addition to the composition pattern, the cluster size can be determined by methods similar to those described above for monometallic particles with the knowledge of the average number of metal–metal neighbours per metal atom,

$$n_{MM} = x_A n_{AM} + x_B n_{BM}. \tag{7}$$

Another similar method to estimate the atomic distribution in a bimetallic cluster has been proposed by Hwang *et al.* (2005). In this method, several parameters were defined:

$$P_{\text{observed}} = \frac{n_{AB}}{n_{AM}}, \qquad R_{\text{observed}} = \frac{n_{BA}}{n_{BM}},$$
$$P_{\text{random}} = \frac{x_B}{x_A + x_B}, \qquad R_{\text{random}} = \frac{x_A}{x_A + x_B}. \tag{8}$$

The extents of alloying of element A (J_A) and B (J_B) were given by

$$J_A = \frac{P_{\text{observed}}}{P_{\text{random}}} \times 100\%, \qquad J_B = \frac{R_{\text{observed}}}{R_{\text{random}}} \times 100\%. \tag{9}$$

Several cases were discussed and here we list five of them. (i) $J_A = 0$ and $J_B = 0 \rightarrow$ separated homometallic clusters.

(ii) $J_A = J_B = 100\% \rightarrow$ perfectly alloyed clusters.

(iii) $J_A < 100\%$ and $J_B < 100\% \rightarrow$ partial A and B atoms tend to segregate; in this case, if $J_A < J_B$ it indicates an A-rich core and a B-rich shell.

(iv) $J_A > 100\%$ and $J_B < 100\% \rightarrow$ both A and B atoms prefer B rather than A.

(v) $J_A > 100\%$ and $J_B > 100\% \rightarrow$ higher ratio of hetero-metallic bonds than homometallic bonds.

To reliably obtain the CNs of metal–metal bonds, the EXAFS fitting should be performed concurrently for both absorption edges with obvious constraints imposed on the heterometallic bonds,

$$n_{AB} = \frac{x_B}{x_A} n_{BA}, \quad R_{AB} = R_{BA}, \quad \sigma_{AB}^2 = \sigma_{BA}^2. \quad (10)$$

To analyze higher-shell data, it is necessary to add the multiple-scattering path contributions, which may be comparable to the amplitude of the single-scattering paths.

3.2. Bimetallic clusters with overlapping absorption edges

Some bimetallic systems contain two elements, for example Ir and Pt, that are close to each other in the periodic table. In this case the EXAFS region of the Ir edge spectrum intrudes into the spectrum of Pt. This phenomenon could be extended to any materials with adjacent absorption edges, for instance, the Ti K edge and Ba L_3 edge of perovskite, $BaTiO_3$. With overlapping XAFS signals, accurately analysing the XAFS data of these systems could be problematic. Separating these EXAFS signals can be performed experimentally in selected cases. As an example, Ravel and coworkers used diffraction anomalous fine-structure (DAFS) measurements to separate the fine-structure signals from barium and titanium (Ravel *et al.*, 1999). In another approach, Glatzel and coworkers used high-energy resolution fluorescence detection, which enables the separation of emission lines from different elements (Glatzel *et al.*, 2005). Here, we introduce an analytical method that can be broadly applied to any combination of elements that have overlapping absorption edges in order to deconvolute their EXAFS signals analytically.

Menard and coworkers reported a new method and successfully deconvoluted the XAFS signals of overlapped Ir and Pt L_3 edges (Menard *et al.*, 2009). The overlapped XAFS signals could be split into three parts: (i) the Ir EXAFS in the Pt L_3 edge before the Pt L_3 edge, (ii) the Ir EXAFS in the Pt L_3 edge and (iii) the Pt EXAFS in the Pt L_3 edge. These three contributions could be described by the EXAFS equations

$$\chi_{\text{Ir edge}}(k_{\text{Ir}}) = \frac{S_{0,\text{Ir}}^2 N_{\text{Ir}}}{k_{\text{Ir}} R_{\text{Ir}}^2} |f_{\text{Ir}}^{\text{eff}}(k_{\text{Ir}})| \sin\left[2k_{\text{Ir}}R_{\text{Ir}} - \frac{4}{3}\sigma_{\text{Ir}}^{(3)}k_{\text{Ir}}^3 + \delta_{\text{Ir}}(k_{\text{Ir}})\right]$$
$$\times \exp(-2\sigma_{\text{Ir}}^2 k_{\text{Ir}}^2) \exp\left[-\frac{2R_{\text{Ir}}}{\lambda_{\text{Ir}}(k_{\text{Ir}})}\right], \quad (11)$$

and

$$\chi_{\text{Pt edge}}(k_{\text{Pt}}, k_{\text{Ir}}) = \frac{S_{0,\text{Pt}}^2 N_{\text{Pt}}}{k_{\text{Pt}} R_{\text{Pt}}^2} |f_{\text{Pt}}^{\text{eff}}(k_{\text{Pt}})|$$
$$\times \sin\left[2k_{\text{Pt}}R_{\text{Pt}} - \frac{4}{3}\sigma_{\text{Pt}}^{(3)}k_{\text{Pt}}^3 + \delta_{\text{Pt}}(k_{\text{Pt}})\right]$$
$$\times \exp(-2\sigma_{\text{Pt}}^2 k_{\text{Pt}}^2) \exp\left[\frac{2R_{\text{Pt}}}{\lambda_{\text{Pt}}(k_{\text{Pt}})}\right]$$
$$+ \frac{A S_{0,\text{Ir}}^2 N_{\text{Ir}}}{k_{\text{Ir}} R_{\text{Ir}}^2} |f_{\text{Ir}}^{\text{eff}}(k_{\text{Ir}})|$$
$$\times \sin\left[2k_{\text{Ir}}R_{\text{Ir}} - \frac{4}{3}\sigma_{\text{Ir}}^{(3)}k_{\text{Ir}}^3 + \delta_{\text{Ir}}(k_{\text{Ir}})\right]$$
$$\times \exp(-2\sigma_{\text{Ir}}^2 k_{\text{Ir}}^2) \exp\left[-\frac{2R_{\text{Ir}}}{\lambda_{\text{Ir}}(k_{\text{Ir}})}\right]. \quad (12)$$

In the process of fitting, appropriate constraints and strategies should be applied.

(i) The nonlinear least-squares fitting of equations (11) and (12) to experimental data should be performed concurrently.

(ii) The factor $A = \Delta\mu_{0,\text{Ir}}/\Delta\mu_{0,\text{Pt}}$, where $\Delta\mu_{0,\text{Ir}}$ and $\Delta\mu_{0,\text{Pt}}$ are the changes in the absorption at the edge steps, is necessary in fitting because the extraction of $\chi(k)$ includes a normalization to these edge steps.

(iii) The correction to the threshold energy (in eV) for the Ir EXAFS at the Pt L_3 edge should be defined as $\Delta E_{0,\text{Ir}} - (349 + \Delta E_{0,\text{Pt}})$, where 349 eV is the difference between the empirical threshold energies. Such a large energy origin shift is necessary in this method since it accounts for a unique $k = 0$ reference point for the Ir EXAFS extending beyond the Pt edge when the Pt edge EXAFS is transformed to k-space.

(iv) Constraints should be made to Ir–M paths because the Ir EXAFS in the Ir L_3 and Pt L_3 edges describe the same coordination environments of Ir atoms.

4. Limitations of EXAFS methods for the analysis of nanoclusters

The artefacts in EXAFS analysis arise owing to the broad range of sizes and compositions of cluster ensembles, and the corrective strategies that should be undertaken are described below. Heterogeneity of bond-length and compositional distributions is a common situation that occurs not only in each individual cluster but can be present due to the changes between multiple clusters. In addition, theoretical calculations reveal the importance of dynamic structural disorder (a contribution of the low-frequency component to the bond dynamics of clusters that may cause shape changes and even mobility over a several picosecond time scale) for the catalytic activity of metal clusters (Rehr & Vila, 2014).

For small clusters, the effects of capping ligands (Carter *et al.*, 1997), steric effects (Shiang *et al.*, 1995), crystalline defects (de la Rubia & Gilmer, 2002) and interaction with adsorbates (López-Cartes *et al.*, 2005) could result in imperfection in the crystalline lattice of clusters. The enhanced surface tension causes a decrease in the lattice parameter (Mays *et al.*, 1968). The bonds near the surface of nanoclusters are more strained than those inside the core, which accordingly results in a

strong variation in the interatomic distances between outside and inside bonds (Huang *et al.*, 2008). Such non-Gaussian or interparticle disorder would cause a problem in EXAFS analysis if it is not considered. Yevick & Frenkel (2010) examined the effects of surface disorder on EXAFS modelling of metallic clusters with 147 and 923 atoms. They applied the empirical distortion function $f(r)$ to each atom within the clusters to simulate surface-tension effects:

$$f(r) = A + (1 - A)\exp(Cr), \quad \text{where } C = \frac{1}{R}\ln\left(\frac{B - A}{1 - A}\right). \tag{13}$$

This distortion function satisfies the conditions $f(0) = 1$ and $f(R) = B \leq 1$ for the atoms at the centre and the periphery, respectively. Multiplying the radial distortion function (equation 13) to all atomic coordinates yields the new positions of atoms in the distorted cluster. The parameter A ($1.00001 \leq A \leq 1.05$) corresponds to the curvature of the distortion curve to simulate the uniformly (Woltersdorf *et al.*, 1981) and nonuniformly distorted structures (Huang *et al.*, 2008). The B parameter lies in the range 0.95–1.0, which agrees well with physically reasonable bond-length truncation effects in small clusters. Fig. 4(*a*) shows the distortion function $f(r)$ with different curvatures A as a function of r/R. Different distortion functions represent different bond-length distributions of the first nearest-neighbour bonds or different radial relaxation of the surface tension within a cluster. The results exhibited the enhanced surface disorder in metal clusters (less than 5 nm). If such disorder is unaccounted for in analysis, it may result in a significant underestimation of the particle size (Fig. 4*b*) and an overestimation of the nearest-neighbour distances. To minimize the errors in the analysis because of surface relaxation, one can passivate the cluster surface with
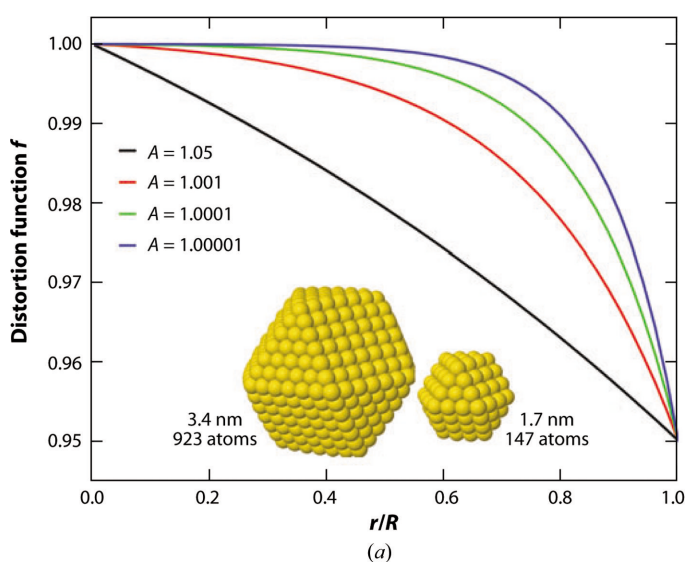
H_2, which increases the bulk-like order in the clusters (Kang *et al.*, 2006; Sanchez *et al.*, 2009), or use complementary techniques, such as the pair distribution function (PDF; Chapman & Chupas, 2013), when the asymmetric disorder causes artefacts in the conventional EXAFS analysis. In 2018, a new method of mapping the EXAFS spectra onto the pair radial distribution function $g(r)$ of neighbours was developed based on the artificial neural network approach (Timoshenko *et al.*, 2018). Utilizing this method, Timoshenko, Frenkel and coworkers obtained the characteristics of monometallic and bimetallic nanoparticles directly from $g(r)$ and observed more detailed information about placement of dilute Pd atoms in the gold-rich nanoparticles than is available through coordination-number analysis (Timoshenko *et al.*, 2019).

Other than the intraparticle disorder, the interparticle disorder also affects the EXAFS results. The general understanding is that the CNs derived from EXAFS analysis overestimate the average cluster size if the size distribution of clusters is broad. To interpret it, Frenkel *et al.* (2011) consider a symmetric arbitrary distribution ρ of cluster order (L) approximated as the Gaussian function,

$$\rho(L) = \exp\left[-\frac{(L - \bar{L})^2}{2\sigma_s^2}\right], \tag{14}$$

where $\bar{L}$ is the average cluster order and σ_s is the standard deviation in L. The average coordination numbers are calculated over all clusters with the size distribution $\rho(L)$:

$$\tilde{n} = \frac{\int_0^\infty \rho(L)N(L)n(L)\,\mathrm{d}L}{\int_0^\infty \rho(L)N(L)\,\mathrm{d}L}. \tag{15}$$

Figure 4
(*a*) Different distortion functions corresponding to $B = 0.95$. Two clusters of different sizes are shown; both are distorted with $A = 1.00001$ and $B = 0.95$. (*b*) Coordination numbers of the first-nearest neighbours obtained with a quasi-Gaussian approximation by a *FEFF*6 fit to the data generated for model clusters of 147 and 923 atoms with different radial distortions A. Best-fit results are shown with symbols, and the model coordination numbers are shown as horizontal dashed lines. The solid lines are guides for the eye. Reprinted with permission from Yevick & Frenkel (2010). Copyright 2010 by the American Physical Society.
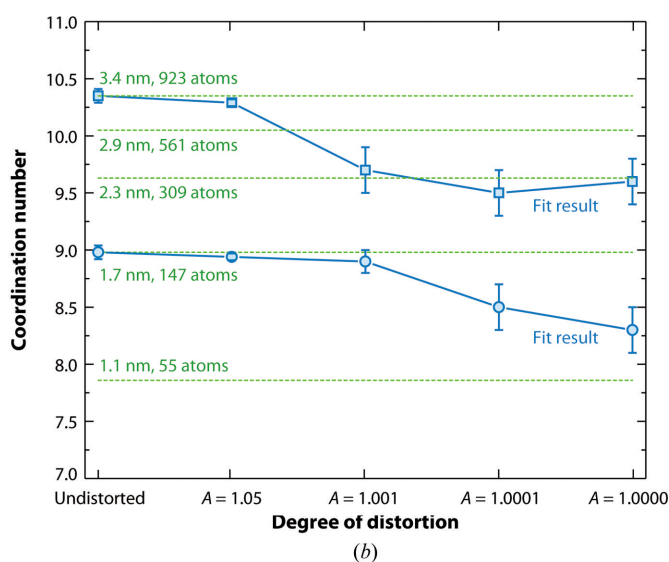
Equation (15) contains a weighting factor, $N(L)$, which indicates the number of atoms in a cluster of order L. This correction is required because $\rho(L)$ is commonly obtained by electron-microscopy measurements as a frequency distribution that depends on cluster size, not volume, whereas volume averaging is required for CN measurements by EXAFS. To estimate the effect of $\rho(L)$ on the average CNs, clusters with cuboctahedral geometry are assumed. The calculated average CNs for various values of $\bar{L}$ as a function of σ_s are plotted in Fig. 5. If $\sigma_s = 0$ (all clusters are identical), $\tilde{n} = n_0$, the CN in each cluster. When σ_s increases $\tilde{n} > n_0$ because the larger clusters contribute more to the average than the smaller clusters. For systems with a relatively narrow size distribution ($\sigma_s < 0.5$ for small clusters and $\sigma_s < 1$ for larger clusters) the EXAFS predictions are not significantly affected (Fig. 5). Frenkel *et al.* (2011) also examined the effects of σ_s on r and σ^2, and observed that even for very poorly defined cluster sizes, with $\sigma_s/L \simeq 2/3$ and typical choices of $r(L)$, the resulting corrections do not exceed 0.015 Å for r and 0.00015 Å^2 for σ^2.

In summary, the following guidance can be offered for the interpretation of the CNs in clusters. (i) If the distribution of particles sizes is known, the theoretical average CN can be obtained by applying equation (15). (ii) For a quasi-Gaussian distribution, the average CN can be determined from Fig. 5 for different values of σ_s. (iii) If σ_s is incorrectly assumed to be too narrow, the EXAFS CNs overestimate the mean cluster size. (iv) A combination of EXAFS and microscopic analyses is necessary to find out whether the models proposed based on each method agree with each other (Agostini *et al.*, 2014). If the EXAFS-derived cluster size is found to be outside the measured size distribution, such a discrepancy suggests that there must be other factors that have not yet been considered, for example the presence of ultrasmall clusters that cannot be directly measured by electron microscopy, or that the wrong model was chosen to describe the EXAFS results. (v) The
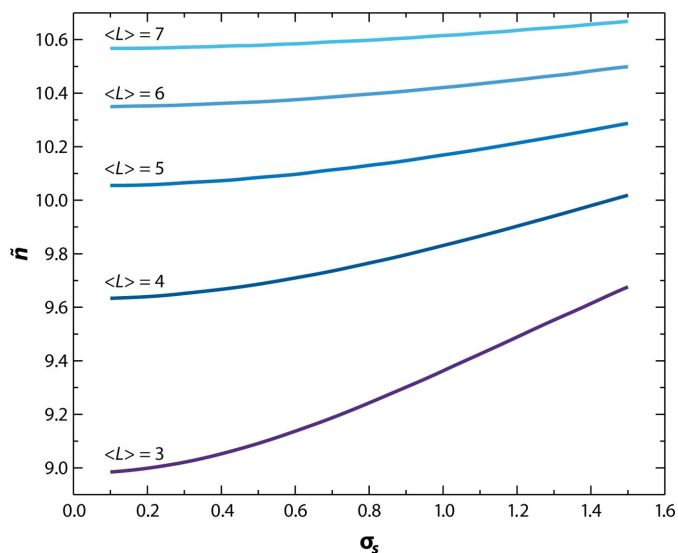
effects of σ_s on r and σ^2 are relatively weak compared with those on the CNs.

Next, we discuss the effects of compositional disorder on the CNs of heterometallic nanoclusters determined by EXAFS analysis. For demonstration, a simple system which contains clusters of the same size but of different compositions is considered. We will assume the distribution of compositions across the ensemble of clusters to be a Gaussian,

$$\rho(x) = \exp\left[-\frac{(x - \bar{x})^2}{2\sigma_c^2}\right], \qquad (16)$$

where $x = N_A/N$ is the fraction of A atoms in each cluster, $\bar{x}$ is the average composition over all clusters and σ_c represents the standard deviation in the distribution of $\rho(x)$. Furthermore, assuming a random ordering of the atoms within each cluster, the partial CN n_{AA} in each cluster is defined as

$$n_{AA} = \frac{N_A - 1}{N - 1} n_{MM}, \qquad (17)$$

where N_A is the number of A atoms in the given cluster and N is the total number of atoms in each cluster. Compared with the equations used by Hwang *et al.* (2005) and Frenkel (2007), which require that $n_{AA} = xn_{MM}$ for randomly distributed atoms within the clusters, equation (17) is more general, is accurate for all clusters and correctly calculates the CNs over the entire compositional range. The exact formulas for the partial CNs, averaged over the ensemble of clusters, are

$$\tilde{n}_{AA} = \frac{\int_0^1 \rho(x) x n_{AA}(x)\, \mathrm{d}x}{\int_0^1 \rho(x) x\, \mathrm{d}x}, \quad \tilde{n}_{AB} = n_{MM} - \tilde{n}_{AA} = n_{AM} - \tilde{n}_{AA}. \qquad (18)$$

For clusters with 100 atoms, calculated partial CNs which have been normalized by n_{MM} are shown in Fig. 6. The results indicate that the ensemble average $\tilde{n}_{AA}$ can be smaller for narrow compositional distributions, or larger for broad distributions, than the CNs predicted by the equation $n_{AA} = xn_{MM}$. The two sets of values, $\tilde{n}_{AA}$ and n_{AA}, agree for $\sigma_c = [x(1 - x)/N]^{1/2}$, for which the normal distribution coincides with the binomial distribution. To summarize, for bimetallic systems with broad composition distributions, corrections can be applied to characterize the equivalent cluster of the samples.

5. Future perspectives

An important limitation in the analysis and modelling of EXAFS data is the ensemble-averaging nature of the technique. A possible remedy is to employ single-nanoparticle spectroscopy (Nie & Emory, 1997; Xu *et al.*, 2008). Xu and coworkers demonstrated the benefit of single-nanoparticle spectroscopy over ensemble-averaging techniques by studying catalysis by a single gold nanoparticle at the single-molecule level. They discovered two distinct nanoparticle groups (about 6 nm) which show different catalytic activities (Xu *et al.*, 2009).
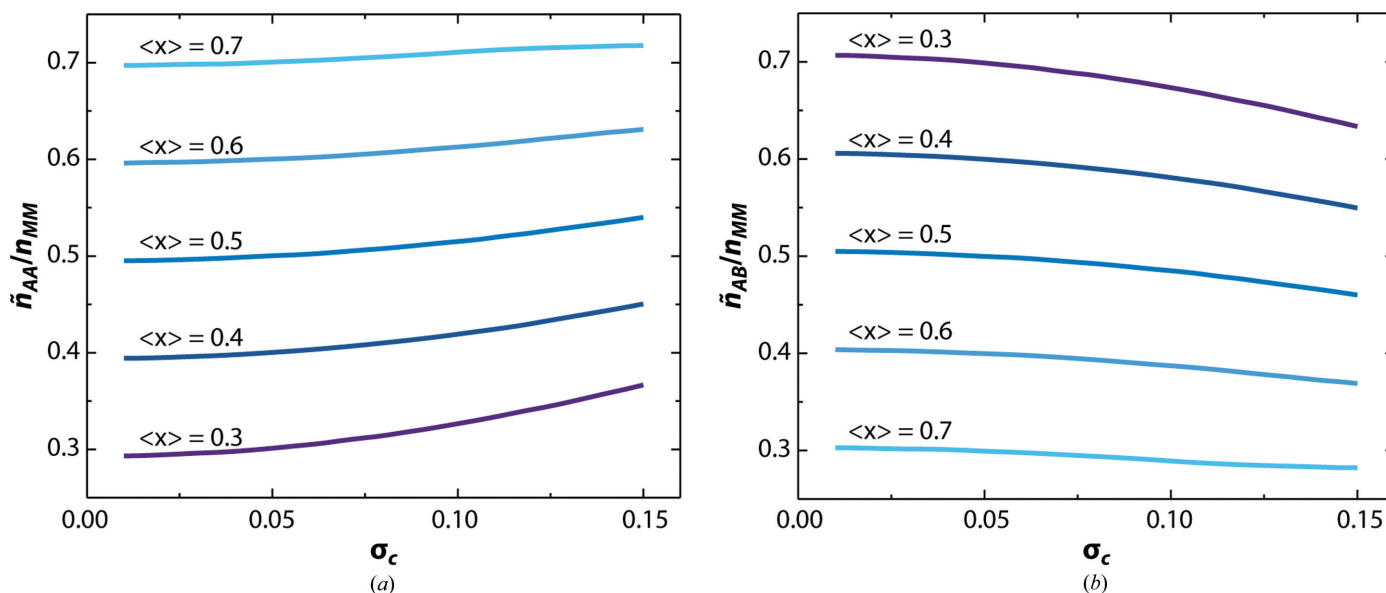

Figure 5
Apparent coordination number ($\tilde{n}$) as a function of the standard deviation of the size distribution (σ_s) for clusters with cuboctahedral geometry. Reproduced with permission from Frenkel *et al.* (2011).

Figure 6
Normalized partial coordination number of (*a*) *AA* and (*b*) *AB* pairs as function of the standard deviation of the cluster composition for clusters of *N* = 100 atoms, calculated assuming a Gaussian compositional distribution. Reproduced with permission from Frenkel *et al.* (2011)

To develop X-ray spectroscopy at the single-particle level, one of the key challenges is the design of the probe. Hitchcock and Toney have published an overview of spectromicroscopy methods that include nanoprobe-based systems (Hitchcock & Toney, 2014). Challenges to the existing nanoprobe methods have been summarized by Frenkel & van Bokhoven (2014).

Characterization of nanoclusters *in situ* or in *operando* conditions is now one of the most important requirements for modern applications of synchrotron-based spectroscopic methods. Accordingly, there are growing demands in developing time-resolved and *operando* techniques. For instance, to bridge the 'pressure gap' between spectroscopic and electromicroscopic techniques, Frenkel, Stach and coworkers demonstrated the advantage of using a micro-reactor for nanocatalysis studies at ambient temperature and pressure (Li *et al.*, 2015; Zhao *et al.*, 2015). The catalytically active site is often only a minority of the atoms in the catalysts, and sensitivity is therefore an issue. Ferri and coworkers employed modulation excitation and filtering of the corresponding spectra with the excitation frequency to increase the sensitivity to the differences in the spectra, which provides a better chance of capturing the structure of the active site selectively (Ferri *et al.*, 2011). Intermediate species can be detected by a phase delay of the structural difference. Pump–probe measurements are able to capture structural variation on microsecond, nanosecond, picosecond and even femtosecond time scales (Bressler & Chergui, 2004). In the literature related to this technique, most such measurements involve a photocatalytic process during which a flash of light induces electron excitation, after which a structural change occurs and is detected in an ultrafast time domain (Bressler *et al.*, 2009; Smolentsev *et al.*, 2014).

To summarize, nanoclusters have been studied for several decades with an increasing accuracy and level of detail that

parallel the development of analytical methods. Of these methods, the X-ray absorption spectroscopy technique has proved to be uniquely capable of capturing multiple attributes of structure and measuring their dynamic changes in real time owing to externally controlled conditions. The combination of the ongoing developments of cluster-synthesis methods, new synchrotron nanoprobe methodologies and the increased use of *in situ*/*operando* characterization techniques are promising new directions for future progress in this field in the next decade.

References

Agostini, G., Piovano, A., Bertinetti, L., Pellegrini, R., Leofanti, G., Groppo, E. & Lamberti, C. (2014). *J. Phys. Chem. C*, **118**, 4085–4094.
Beale, A. M. & Weckhuysen, B. M. (2010). *Phys. Chem. Chem. Phys.* **12**, 5562–5574.
Bressler, C. & Chergui, M. (2004). *Chem. Rev.* **104**, 1781–1812.
Bressler, C., Milne, C., Pham, V.-T., Elnahhas, A., van der Veen, R. M., Gawelda, W., Johnson, S., Beaud, P., Grolimund, D., Kaiser, M., Borca, C. N., Ingold, G., Abela, R. & Chergui, M. (2009). *Science*, **323**, 489–492.
Brown, M. A., Jordan, I., Beloqui Redondo, A., Kleibert, A., Wörner, H. J. & van Bokhoven, J. A. (2013). *Surf. Sci.* **610**, 1–6.
Calvin, S., Miller, M. M., Goswami, R., Cheng, S.-F., Mulvaney, S. P., Whitman, L. J. & Harris, V. G. (2003). *J. Appl. Phys.* **94**, 778–783.

Carter, A. C., Bouldin, C. E., Kemner, K. M., Bell, M. I., Woicik, J. C. & Majetich, S. A. (1997). *Phys. Rev. B*, **55**, 13822–13828.

Chapman, K. W. & Chupas, P. J. (2013). *In-situ Characterization of Heterogeneous Catalysts*, edited by J. A. Rodriguez, J. C. Hanson & P. J. Chupas, pp. 147–168. Hoboken: John Wiley & Sons.

Cowley, J. M. (1950). *Phys. Rev.* **77**, 669–675.

Diaz de la Rubia, T. & Gilmer, G. (2002). *Nat. Mater.* **1**, 89–90.

Ferri, D., Newton, M. A. & Nachtegaal, M. (2011). *Top. Catal.* **54**, 1070–1078.

Frenkel, A. (2007). *Z. Kristallogr.* **222**, 605–611.

Frenkel, A., Frankel, S. & Liu, T. (2005). *Phys. Scr.* **2005**, 721.

Frenkel, A. I. (1999). *J. Synchrotron Rad.* **6**, 293–295.

Frenkel, A. I. (2012). *Chem. Soc. Rev.* **41**, 8163–8178.

Frenkel, A. I., Cason, M. W., Elsen, A., Jung, U., Small, M. W., Nuzzo, R. G., Vila, F. D., Rehr, J. J., Stach, E. A. & Yang, J. C. (2014). *J. Vac. Sci. Technol. A*, **32**, 020801.

Frenkel, A. I., Hills, C. W. & Nuzzo, R. G. (2001). *J. Phys. Chem. B*, **105**, 12689–12703.

Frenkel, A. I., Menard, L. D., Northrup, P., Rodriguez, J. A., Zypman, F., Glasner, D., Gao, S.-P., Xu, H., Yang, J. C. & Nuzzo, R. G. (2007). *AIP Conf. Proc.* **882**, 749–751.

Frenkel, A. I. & van Bokhoven, J. A. (2014). *J. Synchrotron Rad.* **21**, 1084–1089.

Frenkel, A. I., Wang, Q., Sanchez, S. I., Small, M. W. & Nuzzo, R. G. (2013). *J. Chem. Phys.* **138**, 064202.

Frenkel, A. I., Yevick, A., Cooper, C. & Vasic, R. (2011). *Annu. Rev. Anal. Chem.* **4**, 23–39.

Ganguly, M., Pal, A., Negishi, Y. & Pal, T. (2013). *Langmuir*, **29**, 2033–2043.

Gates, B. C. (1995). *Chem. Rev.* **95**, 511–522.

Glasner, D. & Frenkel, A. I. (2007). *AIP Conf. Proc.* **882**, 746–748.

Glatzel, P., de Groot, F. M. F., Manoilova, O., Grandjean, D., Weckhuysen, B. M., Bergmann, U. & Barrea, R. (2005). *Phys. Rev. B*, **72**, 014117.

Hansen, P. L., Wagner, J. B., Helveg, S., Rostrup-Nielsen, J. R., Clausen, B. S. & Topsøe, H. (2002). *Science*, **295**, 2053–2055.

Hitchcock, A. P. & Toney, M. F. (2014). *J. Synchrotron Rad.* **21**, 1019–1030.

Huang, W. J., Sun, R., Tao, J., Menard, L. D., Nuzzo, R. G. & Zuo, J. M. (2008). *Nat. Mater.* **7**, 308–313.

Hwang, B.-J., Sarma, L. S., Chen, J.-M., Chen, C.-H., Shih, S.-C., Wang, G.-R., Liu, D.-G., Lee, J.-F. & Tang, M.-T. (2005). *J. Am. Chem. Soc.* **127**, 11140–11145.

Jentys, A. (1999). *Phys. Chem. Chem. Phys.* **1**, 4059–4063.

Johnston, R. L. (2002). *Atomic and Molecular Clusters.* London: Taylor & Francis.

Kang, J. H., Menard, L. D., Nuzzo, R. G. & Frenkel, A. I. (2006). *J. Am. Chem. Soc.* **128**, 12068–12069.

Li, Y., Zakharov, D., Zhao, S., Tappero, R., Jung, U., Elsen, A., Baumann, P., Nuzzo, R. G., Stach, E. A. & Frenkel, A. I. (2015). *Nat. Commun.* **6**, 7583.

Lin, C.-A. J., Yang, T.-Y., Lee, C.-H., Huang, S. H., Sperling, R. A., Zanella, M., Li, J. K., Shen, J.-L., Wang, H.-H., Yeh, H.-I., Parak, W. J. & Chang, W. H. (2009). *ACS Nano*, **3**, 395–401.

López-Cartes, C., Rojas, T. C., Litrán, R., Martínez-Martínez, D., de la Fuente, J. M., Penadés, S. & Fernández, A. (2005). *J. Phys. Chem. B*, **109**, 8761–8766.

Mays, C. W., Vermaak, J. S. & Kuhlmann-Wilsdorf, D. (1968). *Surf. Sci.* **12**, 134–140.

McKale, A. G., Veal, B. W., Paulikas, A. P., Chan, S.-K. & Knapp, G. S. (1988). *Phys. Rev. B*, **38**, 10919–10921.

Menard, L. D., Wang, Q., Kang, J. H., Sealey, A. J., Girolami, G. S., Teng, X., Frenkel, A. I. & Nuzzo, R. G. (2009). *Phys. Rev. B*, **80**, 064111.

Menard, L. D., Xu, H., Gao, S.-P., Twesten, R. D., Harper, A. S., Song, Y., Wang, G., Douglas, A. D., Yang, J. C., Frenkel, A. I., Murray, R. W. & Nuzzo, R. G. (2006). *J. Phys. Chem. B*, **110**, 14564–14573.

Montejano-Carrizales, J. M., Aguilera-Granja, F. & Morán-López, J. L. (1997). *Nanostruct. Mater.* **8**, 269–287.

Nashner, M. S., Frenkel, A. I., Adler, D. L., Shapley, J. R. & Nuzzo, R. G. (1997). *J. Am. Chem. Soc.* **119**, 7760–7771.

Nie, S. & Emory, S. R. (1997). *Science*, **275**, 1102–1106.

Ravel, B., Bouldin, C. E., Renevier, H., Hodeau, J.-L. & Berar, J.-F. (1999). *J. Synchrotron Rad.* **6**, 338–340.

Rehr, J. J., Booth, C. H., Bridges, F. & Zabinsky, S. I. (1994). *Phys. Rev. B*, **49**, 12347–12350.

Rehr, J. J. & Vila, F. D. (2014). *J. Chem. Phys.* **140**, 134701.

Roldan Cuenya, B., Croy, J. R., Mostafa, S., Behafarid, F., Li, L., Zhang, Z., Yang, J. C., Wang, Q. & Frenkel, A. I. (2010). *J. Am. Chem. Soc.* **132**, 8747–8756.

Sanchez, S. I., Menard, L. D., Bram, A., Kang, J. H., Small, M. W., Nuzzo, R. G. & Frenkel, A. I. (2009). *J. Am. Chem. Soc.* **131**, 7040–7054.

Sasaki, K., Kuttiyiel, K. A., Barrio, L., Su, D., Frenkel, A. I., Marinkovic, N., Mahajan, D. & Adzic, R. R. (2011). *J. Phys. Chem. C*, **115**, 9894–9902.

Shiang, J. J., Kadavanich, A. V., Grubbs, R. K. & Alivisatos, A. P. (1995). *J. Phys. Chem.* **99**, 17417–17422.

Smolentsev, G., Guda, A. A., Janousch, M., Frieh, C., Jud, G., Zamponi, F., Chavarot-Kerlidou, M., Artero, V., van Bokhoven, J. A. & Nachtegaal, M. (2014). *Faraday Discuss.* **171**, 259–273.

Sun, S., Murray, C. B., Weller, D., Folks, L. & Moser, A. (2000). *Science*, **287**, 1989–1992.

Tao, F., Grass, M. E., Zhang, Y., Butcher, D. R., Renzas, J. R., Liu, Z., Chung, J. Y., Mun, B. S., Salmeron, M. & Somorjai, G. A. (2008). *Science*, **322**, 932–934.

Timoshenko, J., Anspoks, A., Cintins, A., Kuzmin, A., Purans, J. & Frenkel, A. I. (2018). *Phys. Rev. Lett.* **120**, 225502.

Timoshenko, J., Wrasman, C. J., Luneau, M., Shirman, T., Cargnello, M., Bare, S. R., Aizenberg, J., Friend, C. M. & Frenkel, A. I. (2019). *Nano Lett.* **19**, 520–529.

Woltersdorf, J., Nepijko, A. S. & Pippel, E. (1981). *Surf. Sci.* **106**, 64–69.

Xu, W., Kong, J. S. & Chen, P. (2009). *Phys. Chem. Chem. Phys.* **11**, 2767–2778.

Xu, W., Kong, J. S., Yeh, Y.-T. E. & Chen, P. (2008). *Nat. Mater.* **7**, 992–996.

Yevick, A. & Frenkel, A. I. (2010). *Phys. Rev. B*, **81**, 115451.

Zhao, S., Li, Y., Stavitski, E., Tappero, R., Crowley, S., Castaldi, M. J., Zakharov, D. N., Nuzzo, R. G., Frenkel, A. I. & Stach, E. A. (2015). *ChemCatChem*, **7**, 3683–3691.

Zheng, H., Smith, R. K., Jun, Y., Kisielowski, C., Dahmen, U. & Alivisatos, A. P. (2009). *Science*, **324**, 1309–1312.